

# Active Range and Bearing-based Radiation Source Localization

Michael S. Lee<sup>1</sup>, Daniel Shy<sup>2</sup>, William “Red” Whittaker<sup>1</sup>, Nathan Michael<sup>1</sup>

**Abstract**—3D radiation source localization is a common task across applications such as decommissioning, disaster response, and security, but traditional count-based sensors struggle to efficiently disambiguate between symmetries in sensor, source, and environment configurations. Recent works have demonstrated successful passive source localization using a bearing sensor called the Compton gamma camera that can image radiation. This paper first presents an approach to mapping the spatial distribution of radiation with a gamma camera to estimate source locations. An active source localization framework is then developed that greedily selects new waypoints that maximize the Fisher Information provided by the camera’s range and bearing observations for source localization. Finally the common assumption of a static step size in between waypoints is relaxed to allow step sizes to adapt online to the observed information. The proposed radiation mapping approach is evaluated in  $5 \times 4 \text{ m}^2$  and  $14 \times 6 \text{ m}^2$  laboratory environments, where multiple point sources were localized to within an average of 0.26 m or 0.6% of the environment dimensions. The active source localization approach is evaluated in simulation and an adaptive step size yields a 27% decrease in the localization time and a 16% decrease in the distance traveled to localize a source in a  $15 \times 15 \times 15 \text{ m}^3$  environment.

## I. INTRODUCTION

Radiation source localization is a common task across applications such as decommissioning of nuclear facilities, disaster response, and security. Count-based radiation detection sensors traditionally used for such tasks (e.g. Geiger-Muller counters and scintillators) only convey point measurements of field strength [1] and may require extensive observations over space and time to estimate source locations. Even with numerous readings, these sensors may fail to locate sources in cluttered 3D environments due to symmetries in sensor, source, and environment configurations.

Methods for radiation field mapping and source localization using these count-based sensors have been studied extensively due to their low cost and ubiquity, but most works rely on limiting assumptions such as a prior knowledge of the number of sources [2], a clutter-free environment with negligible attenuation [3–5], or a 2D environment [6].

The recent commercialization of a sensor called the Compton gamma camera that can image the direction of origin of incident gamma photons presents new opportunities for efficient radiation mapping and source localization. Passive 3D radiation mapping of a cluttered environment was recently demonstrated through the iterative triangulation of bearing measurements made by a gamma camera along hand-carried and teleoperated trajectories [7]. This work advances the state

of the art by applying the gamma camera in an active source localization framework.

Successful target localization with bearing-only sensors fundamentally relies on maneuverability to ensure observability [8]. A common objective used in trajectory generation is the maximization of a Fisher Information Matrix (FIM) measure [8–12]. The Fisher Information is also chosen as the objective in this paper for two reasons. First, the Cramer-Rao lower bound proves that the inverse of the Fisher Information Matrix is the minimum covariance achievable by an unbiased estimator [13]. Second, it has also been shown to yield inward spiraling trajectories [10, 12, 14] that both reduce the distance to the source and allow for bearing observations with sufficient angular separation for triangulation. The paper provides three contributions:

- An approach to mapping the spatial distribution of radiation using observations from a gamma camera is introduced. The approach is validated with experiments conducted in  $5 \times 4 \text{ m}^2$  and  $14 \times 6 \text{ m}^2$  laboratory environments, localizing multiple sources to within an average of 0.26 m or 0.6% of the environment dimensions.
- An active source localization framework based on the Fisher Information Matrix is developed to generate optimal trajectories. While previous works have derived the FIM for range-only [14] and bearing-only [10] sensors for motion in a single plane, this paper develops a joint framework for the range and bearing-based nature of gamma camera observations to generate 3D paths.
- The standard assumption of a fixed distance between waypoints [10, 14] (i.e. step size) is relaxed, and the step size is allowed to adapt online to the observed information. The benefits of an adaptive step size are demonstrated in simulation, which leads to a 27% decrease in localization time and a 16% decrease in the distance traveled for the scenarios considered.

## II. METHODOLOGY

This paper addresses the perception and control necessary for active 3D radiation source localization. First, a radiation mapping framework that leverages the bearing observations of a gamma camera is developed. The map is represented as a voxel grid of radiation occupancy probabilities that is thresholded for source location estimates. A control law that maximizes the range and bearing Fisher Information of the estimated source location throughout the camera’s trajectory is formulated. Finally, the trajectory is observed to be highly sensitive to step size and a policy for adapting the step size with the observed information is proposed.

\*This work was supported by DOE-EM under award DE-EM0004067

<sup>1</sup>M. Lee, R. Whittaker, and N. Michael are with the Robotics Institute at Carnegie Mellon University ml5@, red@, nmichael@cmu.edu

<sup>2</sup>D. Shy is with the Department of Nuclear Engineering and Radiological Sciences at the University of Michigan shyd@umich.edu

### A. Radiation Mapping using a Gamma Camera

1) *Compton Gamma Camera*: A gamma camera not only provide the count and energy of incident gamma photons but also their direction of origin through Compton imaging. Compton imaging in turn relies on the physics of Compton scattering, in which a photon collides with an electron in its path, deposits a portion of its energy, and deflects in a new direction. Given the incident photon energy, deposited energies, and interaction locations, Compton scattering physics constrains the incident direction to a cone (as shown in Fig. 1) [15]. As the camera dwells and images at a waypoint, many such Compton cones will accumulate and converge to the direction of the radiation source.

This work uses a Polaris-H sensor, which detects the locations of interactions and the deposited energies necessary for Compton imaging using a  $2 \times 2 \times 1.5 \text{ cm}^3$  CdZnTe crystal. In what is known as an event, an incident gamma photon may interact  $m$  times in the crystal and deposit  $E_1, E_2, \dots, E_m$  energies.  $N$  events observed by the sensor between time indices  $t-1$  and  $t$  will be grouped in sequence in list-mode format as  $\mathbf{z}^{(t)} = \{\mathbf{z}_1^{(t)}, \mathbf{z}_2^{(t)}, \dots, \mathbf{z}_N^{(t)}\}$  where  $\mathbf{z}_n^{(t)} \in \mathbb{R}^{m \times 4}$ ,  $m \in \mathbb{N}$ . Each event is represented as an  $m \times 4$  matrix, where each row records the discretized x, y, z coordinates and deposited energy  $E$  of an interaction.

2) *Radiation Imaging*: The operation of the gamma camera can be described at a high level as a response function that maps radiation source distribution in its environment to corresponding sensor observations. This is captured by the equation below with the source distribution  $m_r \in \mathbb{R}^{J \times 1}$ , the sensor model  $O \in \mathbb{R}^{I \times J}$ , and the likelihood of possible sensor observations  $\bar{\mathbf{z}} \in \mathbb{R}^{I \times 1}$

$$\bar{\mathbf{z}} = O \cdot m_r \quad (1)$$

where the environment is discretized into  $J$  voxels, and  $m_{r_j}$  is the number of photons emitted from voxel  $j$ .  $I$  is the space of all possible events (i.e. combinations of possible interaction locations and energies) and  $\bar{z}_i \in \bar{\mathbf{z}}$  is the expected number of times the  $i$ th event is observed. To solve for the source distribution, two items are needed: the sensor model and a method of inferring  $m_r$  given  $\bar{\mathbf{z}}$ .

The sensor model  $o_{ij}$  is the probability that a photon from voxel  $j$  is detected as the event  $z_i$  (i.e.  $p(\bar{z}_i \geq 1 | m_{r_j} = 1) = o_{ij}$ ). The analytical sensor model used in this paper is derived in [15], which accounts for the inverse square

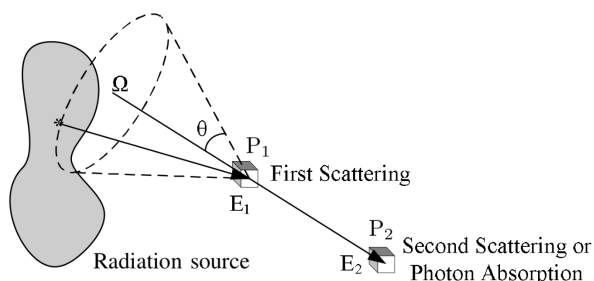


Fig. 1: Physics constrains the incident direction of a photon that Compton scatters at two or more interaction locations ( $P_1, P_2$ ) and energies ( $E_1, E_2$ ) to lie along a cone along with axis  $\Omega$  and opening angle  $\theta$ . [15]

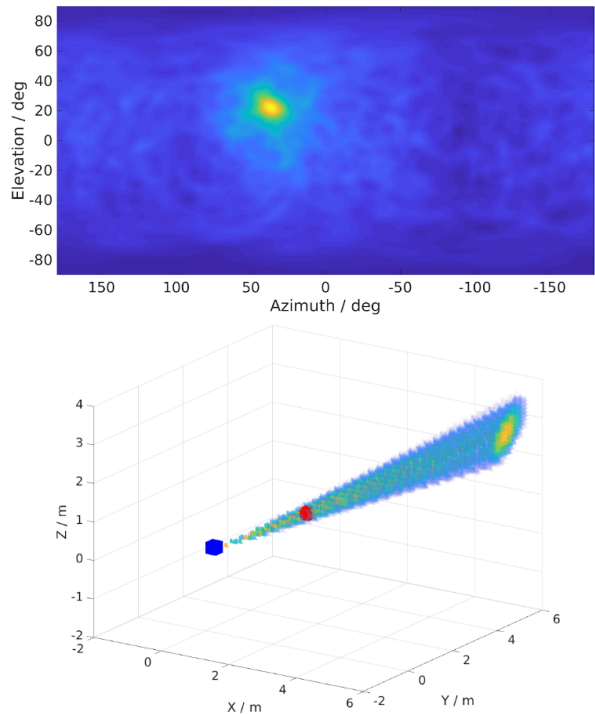


Fig. 2: **Top:** 2D MLEM radiation image of a single source in front of the detector at 45 degrees azimuth and 23 degrees elevation. **Bottom:** Corresponding 3D MLEM radiation image, where the detector is shown as a blue cube, source is shown as a red sphere. Voxels are colored from yellow to blue, corresponding to the probability being along the source direction (only voxels with  $p > 0.9$  are shown).

law radiation, the probabilities of Compton scattering and photoelectric absorption, and the shape of the Compton cone. The extensive model is omitted here for brevity.

Once the analytical sensor model has been calculated for each of the observed events  $\mathbf{z}_n$  in the list-mode data  $\mathbf{z}$ , an iterative imaging algorithm called Maximum Likelihood Expectation Maximization (MLEM) can be applied to infer the source distribution that likely gave rise to the sensor observations [15]. MLEM can be adapted to work in a 2D imaging space to create an image or a 3D imaging space to create a voxel grid-based map. The algorithm is again omitted here for brevity. Examples of 2D and 3D MLEM images from the same dwell point are shown in Fig. 2.

In contrast to count-based sensors that infer range based on the number of observed counts, source source strength, and intermediate attenuation, gamma cameras can determine the direction of the source without any assumptions on the aforementioned quantities. Radiation images taken at distinct locations can then be used to triangulate the source location. This not only enables operation in a broader class of environments, but also allows the peaks of the radiation maps to be approximated as source locations with fewer assumptions on the source and environment configurations.

3) *Radiation Mapping*: The radiation distribution is modeled as a voxel grid with  $J$  voxels that each maintain a probability of containing a source as  $\mathbf{m}_p = \{m_{p_1}, m_{p_2}, \dots, m_{p_J}\}$ . To build a 3D map from 2D images, each voxel is updated with the occupancy probability of the corresponding 2D image pixel that lies along the same spherical direction.

---

**Algorithm 1** Updating Radiation Map

---

```

1: procedure UPDATERMAP( $\mathbf{m}_p^{(t-1)}, \mathbf{p}^{(t)}, \mathbf{z}^{1:t}, \mathbf{T}^{1:t}$ )
2:    $counts = length(\mathbf{z}_t)$ 
3:    $total\_counts = \sum_{k=1}^{t-1} length(\mathbf{z}^{(k)})$ 
4:    $\alpha_c = \frac{counts}{T_t - T_{t-1}}$ 
5:    $\alpha_t = \frac{counts}{T_t - T_1}$ 
6:   for all  $j$  do
7:     if  $p_{jt} \geq occupancy\_threshold$  then
8:        $m_{pj}^{(t)} = m_{pj}^{(t-1)} + \alpha_c \cdot (p_j^{(t)} - m_{pj}^{(t-1)})$ 
9:     else
10:       $m_{pj}^{(t)} = m_{pj}^{(t-1)} + \alpha_t \cdot (p_j^{(t)} - m_{pj}^{(t-1)})$ 
11:    end if
12:   end for
13: end procedure

```

---

As MLEM associates a portion of the total number of detected events in  $\mathbf{z}^{(t)}$  at time  $t$  to each of the  $J$  voxels as  $m_{r_j}$  (see Eq. 1), the following is proposed as the probability of occupancy

$$p(m_{r_j}^{(t)} | \mathbf{z}^{(t)}) = \frac{m_{r_j}^{(t)}}{\max_j(m_{r_j}^{(t)})} = p_j^{(t)} \quad (2)$$

If no counts are observed, then  $p(m_{r_j}^{(t)} | \mathbf{z}^{(t)}) = 0$ .

To incorporate  $p_j^{(t)}$  into the map, a threshold is used to first classify the probabilities into “positive” and “negative” measurements of source occupancy. “Positive” measurements are scaled by the number of counts received in  $\mathbf{z}^{(t)}$  and “negative” measurements are scaled by the duration of  $\mathbf{z}^{(t)}$  as counts and time are the units of information for presence and absence of sources, respectively.

A voxel grid-based radiation map  $m_p$  is updated with the new probabilities of occupancy  $\mathbf{p}^{(t)}$  obtained from the sensor observations  $\mathbf{z}^{(t)}$  following Alg. 1.  $\mathbf{T}^{1:T}$  denotes the dwell times associated with the sensor observations  $\mathbf{z}^{1:t}$ . Under the assumptions of no state uncertainty and no measurement uncertainty, the map update simplifies to a moving average update that is computationally light and amenable to real-time performance.

### B. Active Source Localization

Observations of a gamma camera are range-dependent as the number of incident photons falls off with the square of the distance, and bearing-dependent as angular separation of measurements must be maximized for triangulation. Thus, the goal of this section is to derive an optimal control law for a gamma camera that greedily maximizes the range and bearing information observed (in the Fisher Information sense) for efficient source localization.

*1) Range and Bearing Sensor Models:* Let  $\mathbf{s} = [s_1, s_2, s_3]^\top \in \mathbb{R}^3$  and  $\mathbf{p} = [p_1, p_2, p_3]^\top \in \mathbb{R}^3$  be the source and sensor locations, respectively. The relative position of the sensor is  $\mathbf{r} = \mathbf{p} - \mathbf{s}$  as illustrated in Fig. 3. Observations are defined as random variables range  $z_R$  and bearing  $z_B$ .

The range sensor model considers the probability of observing a given number of photons. Let  $Q_0$  be the known rate of photons incident on the detector 1 m away from the source and  $\Delta t$  be the dwell time of the sensor a distance  $\|\mathbf{r}\|$  away from the source. Accounting for the inverse square

law of attenuation of radiation, the sensor can be expected to observe the following number photons

$$\mu_R(\mathbf{r}) = \frac{Q_0 \Delta t}{\|\mathbf{r}\|^2} \quad (3)$$

where  $\|\cdot\|$  represents the 2-norm.

Though the decay of a source is commonly modeled as Poisson distributed with mean  $\mu$ , a Gaussian distribution with mean and variance  $\mu$  is a good approximation whenever  $\mu > 20$  [1]. As common lab sources between 1  $\mu\text{Ci}$  to 100  $\mu\text{Ci}$  emit tens of thousands to millions of photons a second, the following Gaussian sensor model is adopted for range

$$p(z_R(\mathbf{r}); \mu_R) \sim \mathcal{N}(\mu_R, \sigma_R^2) \quad (4)$$

The bearing to the source provided by a radiation image can be expressed in the source frame with the azimuth and elevation angles  $\Psi$  and  $\Phi$  (see Fig. 3).

$$\mu_B = \begin{bmatrix} \Psi \\ \Phi \end{bmatrix} = \begin{bmatrix} \tan^{-1}(\frac{r_2}{r_1}) \\ \tan^{-1}\left(\frac{r_3}{\sqrt{r_1^2 + r_2^2}}\right) \end{bmatrix} \quad (5)$$

Dwell times can be varied to ensure that a sufficient number of photons are observed to image the bearing to a source with a desired variance  $\sigma_B^2$  (higher observed counts correlate to lower image variance). Assuming an omnidirectional field of view with minimal directional bias, a Gaussian sensor model is once again assumed. Thus, the same analytical sensor model that was used in [10] is used here.

$$p(z_B; \mu_B, \sigma_B^2) \sim \mathcal{N}(\mu_B, \sigma_B^2) \quad (6)$$

*2) Motion Model:* A robot that travels a distance  $d_t$  along a constant azimuth  $\psi_t$  and elevation  $\phi_t$  between waypoints  $\mathbf{p}_t$  and  $\mathbf{p}_{t+1}$  can be modeled with the following kinematics

$$\mathbf{p}_{t+1} = \mathbf{p}_t + \left( d_t \begin{bmatrix} \cos(\phi_t) \cos(\psi_t) \\ \cos(\phi_t) \sin(\psi_t) \\ \sin(\phi_t) \end{bmatrix} \right) \quad (7)$$

where  $\psi_t$  and  $\phi_t$  are defined in a stationary inertial frame.

*3) Fisher Information Matrix (FIM) Derivation:* Candidate waypoints are evaluated based on their expected FIM. The FIM of a sensor model  $p(z(\mathbf{p})|\mathbf{s})$  at a waypoint  $\mathbf{p}$  about the source location  $\mathbf{s}$  is defined as follows

$$FIM(\mathbf{s}, \mathbf{p}) = \mathbb{E}\{[\nabla_{\mathbf{s}} \ln p(z(\mathbf{p})|\mathbf{s})][\nabla_{\mathbf{s}} \ln p(z(\mathbf{p})|\mathbf{s})]^\top\} \quad (8)$$

where  $\nabla$  is the gradient operator.

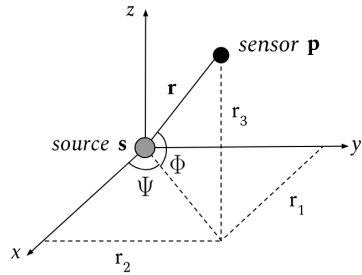


Fig. 3: Bearing (azimuth  $\Psi$ , elevation  $\Phi$ ) and displacement ( $r_1, r_2, r_3$ ) of sensor with respect to source.

The FIM for an N-dimensional Gaussian with constant variance,  $X \sim N(\bar{\mu}(\theta), \Sigma)$ , that is parameterized by K-dimensional parameter vector  $\theta = [\theta_1, \dots, \theta_K]^\top$ , has the following analytical form for the element in the  $i$ th row and  $j$ th column (where  $1 \leq i, j \leq K$ )

$$FIM_{(i,j)} = \frac{\partial \bar{\mu}}{\partial \theta_i} \Sigma^{-1} \frac{\partial \bar{\mu}}{\partial \theta_j} \quad (9)$$

Adapting Eq. 9 for the range sensor model and the source parameter vector  $s$  evaluates to

$$FIM_R(\mathbf{r}) = 4Q_0 \Delta t \frac{\mathbf{r}\mathbf{r}^\top}{(\mathbf{r}^\top \mathbf{r})^3} \quad (10)$$

Similarly, adapting Eq. 9 for the bearing sensor model evaluates to

$$FIM_B(\mathbf{r}) = \frac{1}{\sigma_B^2} \left( \frac{\tilde{\mathbf{r}}\tilde{\mathbf{r}}^\top}{\tilde{\mathbf{r}}^\top \tilde{\mathbf{r}}} + \frac{\check{\mathbf{r}}\check{\mathbf{r}}^\top \oslash \hat{\mathbf{r}}^\top \hat{\mathbf{r}}}{\mathbf{r}^\top \mathbf{r}} \right) \quad (11)$$

where  $\tilde{\mathbf{r}} = [r_2, -r_1, 0]^\top$ ,  $\check{\mathbf{r}} = [r_1 r_3, r_2 r_3, -\sqrt{r_1^2 + r_2^2}]^\top$ ,  $\hat{\mathbf{r}} = [\sqrt{r_1^2 + r_2^2}, \sqrt{r_1^2 + r_2^2}, 1]$ , and  $\oslash$  denotes the Hadamard division.

*4) Control:* Scalar measures of  $FIM_R$  and  $FIM_B$  that encourage measurements that approach the source and obtain sufficient angular separation for triangulation are sought, which leads to the following objective function

$$J(\psi, \phi, d) = \ln \text{tr}(FIM_R) - \ln \text{tr}(FIM_B^{-1}) \quad (12)$$

The trace taken of  $FIM_R$  (T-optimality) is sensitive only to the gross distance to the source and favors the shortest path to the source. However, such a motion collapses a 3D source localization problem into a 1D line search and leaves some source parameters unobservable. The trace of the inverse FIM (A-optimality) complements by minimizing the average variance of the source parameter estimates and encouraging spiraling motions that render all source parameters observable [10]. Finally, the logs help scale the two measures, whose operating range can vary in orders of magnitude across a single mission due to the inverse square law decay and optimization of near-singular matrices of potential waypoints.

The controller greedily maximizes the proposed objective over a single step of a given step size  $d_t$  to determine the next dwell location. This takes the form of an optimization over the heading angles  $\psi_t, \phi_t$

$$[\psi^*, \phi^*] = \arg \max_{\psi, \phi} J(\psi, \phi, d) \quad (13)$$

*5) Fixed Step Size:* The step size between waypoints is a key parameter that implicitly determines the relative scaling between  $FIM_R$  and  $FIM_B$  and consequently the shape of the trajectory. Eq. 10 and 11 reveal that  $FIM_R$  and  $FIM_B$  roughly scale linearly with the cross distance ( $xx^\top$ ) and with the third and second order of the squared distance ( $x^\top x$ ) respectively. As noted in [14], the squared terms draw the sensor directly to the source while the cross terms induce a circling behavior. This can be observed in Fig. 4 where incremental increases in step size yield allow the squared terms to dominate and assert a more direct approach toward the source. Although the relative weighting between  $FIM_R$

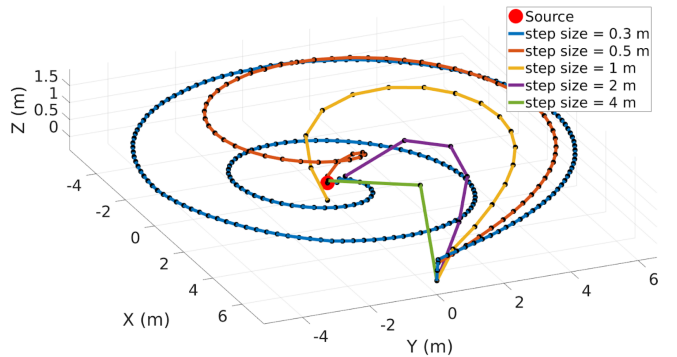


Fig. 4: FIM-optimal trajectories with varying step sizes between 0.3 m to 4 m for a 500  $\mu\text{Ci}$  source. Waypoints are marked with circles. As step size is increased, the trajectory takes a progressively direct approach to the source.

and  $FIM_B$  can be modified by a tradeoff parameter to shape the trajectories, none was used in this paper.

*6) Adaptive Step Size:* Heuristics such as the step size and planning horizon are commonly set to an empirical value that yields good performance [14, 16–18]. Some works, however, adapt these heuristics online, as in [19, 20], where the planning horizon is increased until sufficient information is gained for robustness to local minima.

The gradient-based source seeking algorithm presented in [21] modifies the usual form of gradient gain coefficients used in literature [22, 23] to scale their search step size inversely with the magnitude of the gradient. Drawing a parallel between the gradient magnitude and information gain, this paper similarly scales the search step size with the observed information as follows

$$d_t^R = \frac{(1 + \xi)^\alpha \exp(-\eta_R \ln \text{tr}(FIM_R))}{(t + 1 + \xi)^\alpha}, t = 0, 1, 2, \dots \quad (14)$$

$$d_t^B = \frac{(1 + \xi)^\alpha \exp(-\eta_B \ln \text{tr}(FIM_B^{-1}))}{(t + 1 + \xi)^\alpha}, t = 0, 1, 2, \dots \quad (15)$$

As in [21],  $\alpha$  is set to 0.602 as recommended in [23], and the aggressiveness factors  $\eta_R$  and  $\eta_B$  and stability factor  $\xi$  are included to control the scale of the step sizes and as inertia against decreasing step sizes over time respectively. Trajectories generated with the averaged adaptive step sizes that balance the objectives of proximity and triangulation are shown in Fig. 5.

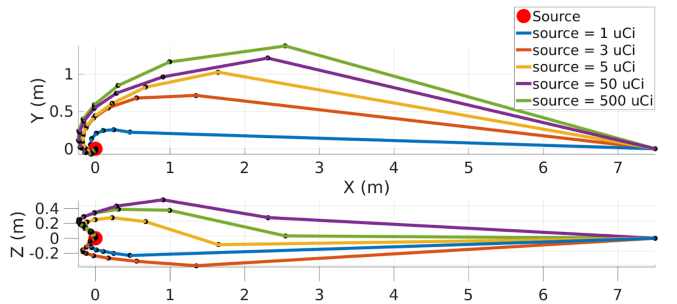


Fig. 5: **Top:** Overhead view of FIM-optimal trajectories using adaptive step sizes for sources with strengths from 1  $\mu\text{Ci}$  to 500  $\mu\text{Ci}$ . Waypoints are marked with circles. Notice that step sizes are adjusted to favor range information for lower strength sources and favor bearing information for those with higher strengths. **Bottom:** Side view.

### III. EXPERIMENTS

This paper presents two sets of experiments that evaluate the proposed radiation mapping and active source localization approaches separately. For the first set of experiments, a ground robot was equipped with a Polaris-H gamma camera to follow a predetermined set of dwells and localize multiple point sources of various isotopes and strengths. The second set of experiments examined the source localization efficiency and accuracy of the developed control law across a range static and adaptive step sizes in simulation.

#### A. Passive Source Localization

Experiments testing the proposed radiation mapping method were conducted in two laboratory environments: a small uncluttered room with  $5 \times 4 \text{ m}^2$  meters of open space, and a large and cluttered room approximately  $14 \times 6 \text{ m}^2$  in size (see Fig. 6 for representative images).

A total of 4 tests were performed in the two environments, where each test varied the robot's trajectory, number of dwells, surrounding point sources, and degree of attenuation. Ground truth measurements of the source locations were recorded to evaluate the accuracy of source locations estimated from LiDAR odometry [24] and MLEM. Details of the four performed experiments can be found in Table I, which compares a baseline, experimental results using the approach described in Section II-A, and simulation results. A voxel size of 10 cm was used for the radiation map.

Quantitatively, sources were localized to an average error of 0.26 m across the conducted tests or 0.6% of the environment dimensions. Qualitatively, the estimated and ground truth source locations are placed in the context of the LIDAR map generated by the robot for tests 3 and 4 in Fig. 7.

For comparison with a count-based source localization method, the particle filter and mean-shift-based algorithm from [25] was implemented due to the minimal assumptions theoretically required for the localization of multiple sources. Each particle is a hypothesis of a source location and strength, and by only updating the weights of particles within a defined radius of a measurement location, an arbitrary number of sources can be localized in largely disjoint regions through mean-shift clustering. For all tests, the measurement radius was set to 5 m and the filter was initialized with 1000 particles uniformly sampled throughout the environment with the correct source strength.

As expected, the baseline performed poorly in the large, cluttered environment with an average localization error of 1.931 m as a result of unmodeled attenuation. The baseline also surprisingly performed poorly in the small, uncluttered environment due to two reasons. The observed count rate is not only dependent on the strength, location, and intermediate attenuation of the source, but also on roughly modeled detector characteristics (e.g. size, intrinsic efficiency) and stochasticity of radioactive decay. Even when all particles were initialized with the correct source strength, the observed count rate rarely matched the expected count rate from particles near the true source location. Second, all radiation measurements were made in a single plane. As a result, particle updates based on the inverse square law could not



Fig. 6: Collage of experiments being carried out in the small (top left and bottom left) and large (right) laboratory environments with a ground robot equipped with a gamma camera.

break the symmetry in the z-axis and struggled to correctly predict the height of the sources.

#### B. Simulation Environment Development and Validation

A radiation simulation environment that models the interaction between gamma photons and the Polaris-H sensor was developed in GEANT4, a particle physics simulator developed by CERN. To validate the developed simulation for active source localization, the experiments were replicated with the same source distribution, dwell times, and dwell points. The comparable results from the simulation are also provided in Table I.

#### C. Active Source Localization

The proposed control law and adaptive step size was evaluated statistically by running a large number of randomized source localization tests. The robot was initialized in a random location in a  $15 \times 15 \times 15 \text{ m}^3$  space to localize a 500  $\mu\text{Ci}$  Cs-137 source placed at the center. 100 tests were run for each of the following step sizes: 1 m, 2 m, 4 m, and adaptive. The following parameters were used for the adaptive step size:  $\eta_R = 0.50$ ,  $\eta_B = 0.15$ ,  $\xi = 50$ ,  $\alpha = 0.602$ , and the map voxels were set to 10 cm. Each test was carried out until the variance of the source localization estimate fell below 0.15 m or 30 minutes had elapsed. Note that the robot dwelled at each waypoint until the number of photons necessary for sufficient resolution of source direction had been observed. The results can be found in Table II.

TABLE I: Passive Source Localization Results

Test	Path (number of dwells*)	Source ( $\mu\text{Ci}$ )	Baseline / Experiment / Simulation Localization Error (m)
1-SM	Straight (6)	Na-22 (61.28)	0.471 / 0.034 / 0.034
2-SM <sup>†</sup>	Straight (6)	Na-22 (61.28)	0.528 / 0.096 / 0.031
3-SM	Lawnmower (11)	Cs-137 (100) Na-22 (61.28) Co-60 (48.60) Ba-133s (82.11)	0.431 / 0.055 / 0.053 0.560 / 0.120 / 0.037 0.516 / 0.105 / 0.089 0.970 / 0.228 / 0.110
4-LG	Coverage (10)	Cs-137 (27.24) Cs-137 (100) Na-22 (61.28) Co-60 (48.60)	3.796 / 0.2621 / 0.0632 2.608 / 1.055 / 1.1859 0.769 / 0.490 / 0.584 0.552 / 0.188 / 0.048

\*All dwells were 1 minute in duration.  
†Attenuation around the source increased from test 1-SM with a lead brick

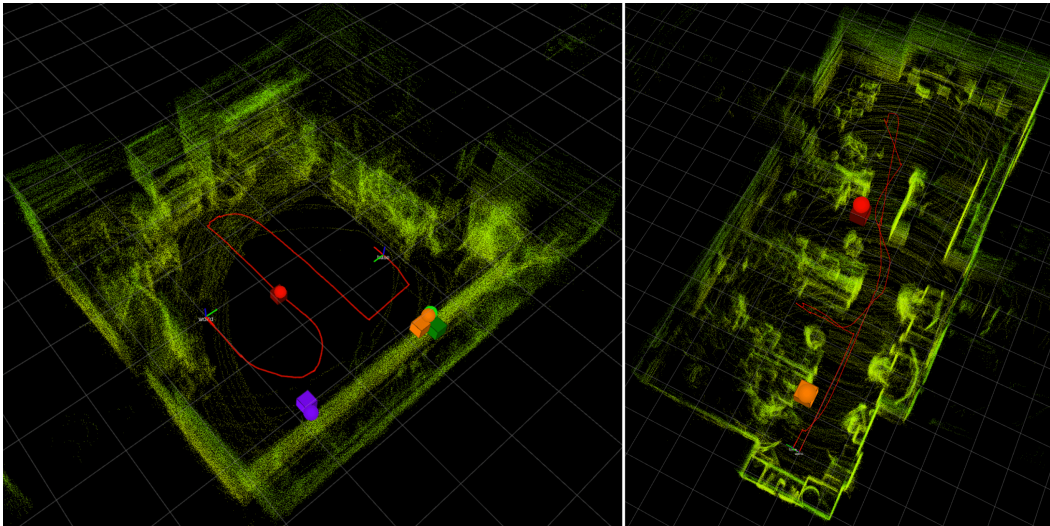


**Fig 7: Left:** Test 3: Estimated locations of Ba-133 (purple), Cs-137 (red), Co-60 (orange), and Na-22 (green) sources are shown as cubes. **Right:** Test 4: Estimated locations of Co-60 (orange) and Na-22 (red) are shown as cubes. **Both:** Ground truth source locations are shown as spheres, with the trajectory of the robot in red and spatial map in green.

TABLE II: Active Source Localization Results

Step Sizes	1 m	2 m	4 m	Adaptive
Rate of success	53%	95%	90%	<b>100%</b>
# Waypoints $[\mu, (\sigma)]$	17.32 (1.01)	11.65 (0.69)	<b>10.29 (0.79)</b>	11.88 (0.97)
Localization error, cm $[\mu, (\sigma)]$	1.40 (1.95)	<b>0.62 (1.74)</b>	2.59 (2.47)	2.50 (2.41)
Total dwell time, min $[\mu, (\sigma)]$	12.47 (2.46)	10.36 (2.54)	9.38 (2.38)	<b>6.88 (1.87)</b>
Distance traveled, m $[\mu, (\sigma)]$	8.16 (1.95)	10.65 (2.15)	18.58 (3.42)	<b>6.87 (1.84)</b>

A fixed step size of 1 m often failed to approach the source quickly enough to localize before the 30-minute time limit. A fixed size of 4 m obtained comparable localization error but at the cost of a high distance traveled as it could not decrease its step size near the source. A fixed size of 2 m had the lowest source localization error as a good compromise between the two static step sizes. However, the adaptive approach had the lowest dwell time and distance traveled for a comparable source localization error as it was able to quickly approach the source then circle the source with smaller step sizes. This flexibility also allowed the adaptive step size to have a 100% completion rate.

#### IV. CONCLUSION

This paper explores an active approach to 3D radiation source localization using a gamma camera. A passive radiation mapping framework that leverages the camera's bearing observations to build a voxel grid of radiation occupancy is first developed. The paper then presents a control law that greedily selects new waypoints that maximize the information provided by the camera's range and bearing observations with respect to the source location estimates obtained by thresholding the occupancy map. Finally the sensitivity of the proposed approach to step size is addressed with a policy that adapts the step size online according to the information observed. Experiments conducted in laboratory environments and in simulation demonstrate the efficacy of the approaches presented to choose efficient, informative 3D paths for accurate source localization.

#### REFERENCES

- [1] G. Knoll, *Radiation detection and measurement*. John Wiley & Sons, 2010.
- [2] M. R. Morelande and A. Skvortsov, "Radiation field estimation using a gaussian mixture," in *FUSION*, 2009, pp. 2247–2254.
- [3] G. Minamoto, E. Takeuchi, and S. Tadokoro, "Estimation of ground surface radiation sources from dose map measured by moving dosimeter and 3D map," *IROS*, 2014.
- [4] M. Morelande, B. Ristic, and A. Gunatilaka, "Detection and parameter estimation of multiple radioactive sources," *FUSION*, 2007.
- [5] J. Towler, B. Krawiec, and K. Kochersberger, "Terrain and Radiation Mapping in Post-Disaster Environments Using an Autonomous Helicopter," *Remote Sensing*, vol. 4, no. 7, pp. 1995–2015, 2012.
- [6] A. Newaz, S. Jeong, H. Lee, H. Ryu, N. Y. Chong, and M. Mason, "Fast radiation mapping and multiple source localization using topographic contour map and incremental density estimation," *ICRA*, 2016.
- [7] K. Vetter, R. Barnowski, A. Haefner, T. Joshi, R. Pavlovsky, and B. Quiter, "Gamma-Ray imaging for nuclear security and safety: Towards 3-D gamma-ray vision," *Nucl. Instrum. Methods Phys. Res.*, 2018.
- [8] J. M. Passerieux and D. Van Cappel, "Optimal observer maneuver for bearings-only tracking," *IEEE Transactions on Aerospace and Electronic Systems*, 2007.
- [9] S. E. Hammel, "Optimal Observer Motion for Bearings-only Localization and Tracking," 1998.
- [10] S. S. Ponda, R. M. Kolacinski, and E. Fazzoli, "Trajectory Optimization for Target Localization Using Small Unmanned Aerial Vehicles," *AIAA guidance, navigation, and control conference*, 2009.
- [11] J. Le Cadre, "Optimization of the Observer Motion for Bearings-Only Target Motion Analysis," pp. 3126–3131, 1997.
- [12] A. N. Bishop and P. N. Pathirana, *Optimal Trajectories for Homing Navigation with Bearing Measurements*. IFAC, 2008, vol. 41, no. 2.
- [13] Y. Bar-Shalom, X. Li, and T. Kirubarajan, *Estimation with applications to tracking and navigation: theory algorithms and software*. John Wiley & Sons, 2004.
- [14] B. Bayat, N. Crasta, H. Li, and A. Ijspeert, "Optimal Search Strategies for Pollutant Source Localization," *IROS*, pp. 1801–1807, 2016.
- [15] D. Xu, "Gamma-ray Imaging and Polarization Measurement using 3-D Position-Sensitive CdZnTe Detectors," 2006.
- [16] G. Ferri, A. Munaf, R. Goldhahn, and K. Lepage, "A Non-Myopic , Receding Horizon Control Strategy for an AUV to Track an Underwater Target in a Bistatic Sonar Scenario," *CDC*, 2014.
- [17] A. Ryan and J. K. Hedrick, "Particle filter based information-theoretic active sensing," *Robotics and Autonomous Systems*, vol. 58, 2010.
- [18] F. Koohifar, A. Kumbhar, and I. Guvenç, "Receding Horizon Multi-UAV Cooperative Tracking of Moving RF Source," *IEEE Commun. Lett.*, vol. 21, 2017.
- [19] B. Charrow, N. Michael, and V. Kumar, "Active Control Strategies for Discovering and Localizing Devices with Range-Only Sensors," *WAFR*, pp. 55–71, 2015.
- [20] J. Tisdale, Z. Kim, and J. K. Hedrick, "Autonomous UAV Path Planning and Estimation," *IEEE Robotics and Automation Magazine*, pp. 35–42, 2009.
- [21] N. Atanasov, J. L. Ny, N. Michael, and G. J. Pappas, "Stochastic Source Seeking in Complex Environments," *ICRA*, pp. 3013–3018, 2012.
- [22] H. Kushner and G. G. Yin, *Stochastic approximation and recursive algorithms and applications*. Springer, 2003, vol. 35.
- [23] J. C. Spall, *Introduction to stochastic search and optimization: estimation, simulation, and control*. John Wiley & Sons, 2005, vol. 65.
- [24] E. Nelson, "Berkeley Localization and Mapping," 2015.
- [25] J. Chin, D. Yau, and N. Rao, "Efficient and robust localization of multiple radiation sources in complex environments," in *ICDCS*, 2011.